Acta Biomaterialia 43 (2016) 262–268

Contents lists available at ScienceDirect

Acta Biomaterialia

journal homepage: www.elsevier.com/locate/actabiomat

Full length article

Functional computer-to-plate near-infrared absorbers as highly efficient photoacoustic dyes

Yuewei Niu [a,b], Wantong Song [a], Dawei Zhang [a], Zhaohui Tang [a,*], Mingxiao Deng [b,*], Xuesi Chen [a]

[a] Key Laboratory of Polymer Ecomaterials, Changchun Institute of Applied Chemistry, Chinese Academy of Sciences, Changchun 130022, PR China
[b] College of Chemistry, Northeast Normal University, Changchun 130024, PR China

ARTICLE INFO

Article history:
Received 9 January 2016
Received in revised form 26 June 2016
Accepted 14 July 2016
Available online 16 July 2016

Keywords:
Photoacoustic imaging
Dye
NIR
Contrast agent

ABSTRACT

Photoacoustic imaging (PAI) is an emerging modality in biomedical imaging. Photoacoustic effect is the basis for PAI, where a photoacoustic contrast agent absorbs optical pulses to initiate localized heating and rapid thermal expansion, thus generating thermoelastic stress waves. Therefore, ideal PAI dyes should have strong NIR light absorbance and high light-heat conversion efficiency. However, most current low molecular weight organic PAI contrast agents are fluorescent dyes, where the light-heat conversion efficiency is dramatically impaired due to the energy loss by fluorescence emission. Herein, we report a series of highly efficient photoacoustic dyes with —COOH, —NH_2 and NHS ester functionalities, from an inexpensive industrial computer-to-plate NIR absorber (IR830 *p*-toluenesulfonate) that has a strong NIR absorbance but an extremely low fluorescence emission. *In vitro* and *in vivo* studies show that the functional IR830 dyes have low cytotoxicity, and are 2.1 folds brighter in photoacoustic imaging than traditional photoacoustic dye indocyanine green (ICG). The Lowest Limit of Quantification of the IR830 series dyes is as low as the 1/7 of that of ICG. These indicate that the functional IR830 dyes have great potential as highly efficient photoacoustic dyes.

Statement of Significance

Photoacoustic imaging (PAI) is an emerging modality in biomedical imaging. Ideal PAI dyes should have strong NIR absorbance and high light-heat conversion efficiency. However, most current low molecular weight organic PAI contrast agents are fluorescent dyes, where the light-heat conversion efficiency is dramatically impaired due to the energy loss by fluorescence emission. Herein we report a series of highly efficient functional photoacoustic dyes from an inexpensive industrial computer-to-plate NIR absorber (IR830) that has a strong NIR absorbance but an extremely low fluorescence emission. The functional IR830 dyes show low cytotoxicity, much brighter in photoacoustic imaging than traditional photoacoustic dye indocyanine green. These indicate that the functional IR830 dyes have great potential as highly efficient photoacoustic dyes.

1. Introduction

Photoacoustic imaging is an emerging modality in biomedical imaging that exhibits strong optical absorption contrast and high ultrasonic resolution, and is becoming increasingly popular as it can overcome the depth and resolution limitations of traditional optical imaging techniques [1–16]. While some endogenous molecules such as haemoglobin and melanin can produce photoacoustic contrast, most biological processes do not cause much variation in the photoacoustic signals. Therefore, it is necessary to develop exogenous contrast agents to improve sensitivity for PAI *in vivo* [17]. A variety of near-infrared (NIR, 650–900 nm) absorptive materials have been developed as exogenous PAI contrast agents. Most of them are organic and inorganic nanomaterials [18], such as carbon nanotubes [19,20], gold [20–22], silver [23], copper [24,25] and magnetic nanoparticles [26]. However, the clinical application of these nanomaterials is severely impaired by their non-biodegradability, poor metabolism and potential long-term toxicity [27]. In comparison, NIR-absorptive low molecular weight organic dyes, such as indocyanine green (ICG) [28–30] and other NIR dyes [31], have demonstrated attractive properties for PAI applications. In particular, ICG has been approved by the FDA for

---

* Corresponding authors.
E-mail addresses: ztang@ciac.ac.cn (Z. Tang), dengmx330@nenu.edu.cn (M. Deng).

http://dx.doi.org/10.1016/j.actbio.2016.07.026

use in humans, which suggests the high clinical translation possibility of similar organic dyes as PAI contrast agents. However, the low photoacoustic efficiency, difficulty of modification, lack of functional groups to label other materials and high cost of these dyes significantly hinder their applications. Therefore, it is highly desirable to develop new functional low molecular weight organic PAI dyes that are highly efficient, yet inexpensive and easily prepared and modified.

Photoacoustic effect is the basis for PAI, where a photoacoustic contrast agent absorbs optical pulses to initiate localized heating and rapid thermal expansion, thus generating thermoelastic stress waves (ultrasound waves) [32]. Therefore, ideal PAI dyes should have strong NIR absorbance and high light-heat conversion efficiency. Most current low molecular weight organic PAI contrast agents are fluorescent dyes [33], where the light-heat conversion efficiency is dramatically impaired due to the energy loss by fluorescence emission. Taking ICG as an example, a large part of the absorbed energy is converted into fluorescence emission but not heat. Thus, the fluorescence property, which has been specially developed for fluorescent dyes, induces an unwanted loss of efficiency in PAI.

IR830 *p*-toluenesulfonate (CAS: 134127-48-3) is an industrial Computer-to-Plate NIR absorber which is inexpensive and readily available. The dye has a strong NIR absorbance but an extremely low fluorescence emission. These properties make IR830 a very attractive option as a potential low molecular weight organic PAI dye. In this study, we have successfully developed a series of functional IR830-based dyes with reactive groups including —COOH, —NH_2 and NHS ester for PAI applications. We further demonstrated that these functional dyes could be conjugated to polymers for *in vivo* PAI in mice, indicating their excellent potential for broad imaging applications.

2. Materials and methods

2.1. Materials

1H-Benz[e]indolium,2-[2-[2-chloro-3-[2-(1,3-dihydro-1,1,3-trimethyl-2H-benz[e]indol-2-ylidene)ethylidene]-1-cyclohexen-1-yl]ethenyl]-1,1,3-trimethyl-,4-methylbenzenesulfonate (IR830 *p*-toluene-sulfonate) was purchased from Liye Chemical Products Technology Development Co., Ltd., China. Amino-terminated poly(ethylene glycol) methyl ether of 5 kDa molecular weight (mPEG5K-NH_2) was purchased from JenKem Technology Co., Ltd., Beijing, China and used without further purification. Poly(L-glutamic acid)-g-methoxy poly(ethylene glycol) (PLG-g-mPEG) was prepared by the reaction of poly(glutamic acid) (M_n 20.7×10^3 g mol^{-1}, PDI 1.36, determined by GPC) with mPEG5K-OH, according to the procedure described in our previous work [34]. The molar ratio of L-glutamic acid units to ethylene glycol units was 1/6.01 in the PLG-g-mPEG copolymer. M_n and PDI of the PLG-g-mPEG were 37.3×10^3 g mol^{-1} and 1.91, respectively. N,N′-dimethylformamide (DMF) was stored over CaH_2 for 3 days and distilled under vacuum prior to use.

2.2. Methods

^{1}H NMR and ^{13}C NMR spectra were recorded on a Bruker AV-400 spectrometer (Bruker, USA). UV–Vis spectra were measured on a UV-2401PC spectrophotometer (Shimadzu, Japan). Fluorescence spectra were obtained at room temperature on a Photon Technology International (PTI, USA) Fluorescence Master System with Felix 4.1.0 software. The HPLC analyses were performed on a Waters 1525 system equipped with a reverse-phase column (Symmetry® C18 4.6 × 250 mm column). Elution was done with eluent A (acetonitrile) and eluent B (methanol) (A/B = 50:50 v/v) pumped at a flow rate of 1.0 mL min^{-1} at 25 °C. The sample injection volume was 20 μL, and the column effluent was detected at 700 nm with a UV/Visible detector (Waters 2489, Waters, USA). Multispectral optoacoustic tomography (MSOT) imaging was performed with an InVision 128 small animal scanner (iThera Medical, GmbH, Neuherberg, Germany).

2.3. Synthesis of IR830 chloride

To a saturated IR830 *p*-toluenesulfonate solution in isopropanol, hydrochloric acid (6 mol/L) was added. IR830 chloride was slowly precipitated from the solution as a red powder. ^{1}H NMR of IR830 *p*-toluenesulfonate (400 MHz, DMSO-d_6): δ 8.33 (dd, 4H, *J* = 17.9, 11.4 Hz), 8.16–8.01 (m, 4H), 7.79 (d, 2H, *J* = 8.9 Hz), 7.66 (t, 2H, *J* = 7.4 Hz), 7.58–7.42 (m, 4H), 7.10 (d, 2H, *J* = 7.9 Hz), 6.35 (d, 2H, *J* = 14.3 Hz), 3.81 (s, 6H), 2.76 (t, 4H, *J* = 5.1 Hz), 2.28 (s, 3H), 1.93 (m, 14H) ppm. ^{1}H NMR of IR830 chloride (400 MHz, DMSO-d_6): δ 8.33 (dd, 4H, *J* = 17.7, 11.5 Hz), 8.16–8.01 (m, 4H), 7.79 (d, 2H, *J* = 8.9 Hz), 7.66 (t, 2H, *J* = 7.6 Hz), 7.53 (t, 2H, *J* = 7.5 Hz), 6.35 (d, 2H, *J* = 14.3 Hz), 3.81 (s, 6H), 2.76 (t, 4H, *J* = 4.5 Hz), 1.92 (m, 14H) ppm.

2.4. Synthesis of IR830-COOH chloride

To a solution of IR830 chloride (1.239 g, 2.00 mmol) in anhydrous DMF (10 mL) were added 3-mercaptopropionic acid (209 μL, 2.40 mmol) and triethylamine (333 μL, 2.40 mmol). The mixture was stirred under nitrogen at room temperature for 20 h in a closed container, then precipitated from ethyl acetate. The solid was collected, dried at room temperature and then re-dissolved in dichloromethane. Then, the solution was washed with brine and the organic extracts were dried over Na_2SO_4, filtered, and concentrated. The concentrated solution was purified by precipitation from diethyl ether to afford the pure IR830-COOH chloride as green powder (1.199 g, yield 87%), 99.4% pure by HPLC, RT 6.93 min. ^{1}H NMR (400 MHz, DMSO-d_6): δ 12.53 (s, 1H), 8.82 (d, 2H, *J* = 14.3 Hz), 8.30 (d, 2H, *J* = 8.5 Hz), 8.08 (t, 4H, *J* = 8.8 Hz), 7.77 (d, 2H, *J* = 8.9 Hz), 7.65 (t, 2H, *J* = 7.4 Hz), 7.51 (t, 2H, *J* = 7.5 Hz), 6.33 (d, 2H, *J* = 14.4 Hz), 3.79 (s, 6H), 3.04 (t, 2H, *J* = 6.6 Hz), 2.70 (t, 4H, *J* = 4.2 Hz), 2.60 (t, 2H, *J* = 6.6 Hz), 1.98 (s, 12H), 1.86 (s, 2H) ppm. ^{13}C NMR (100 MHz, DMSO-d_6): δ 173.54, 172.39, 153.73, 143.62, 140.53, 133.12, 132.85, 131.35, 130.23, 129.90, 127.68, 127.47, 124.75, 122.23, 111.61, 101.25, 50.40, 34.62, 32.41, 31.70, 26.79, 25.75, 20.62 ppm. MALDI-TOF-MS (ES$^+$): *m*/*z* calcd. for [M-Cl]$^+$, 653.32; found, 653.4.

2.5. Synthesis of IR830-B-NH_2 chloride

To a solution of IR830 chloride (1.239 g, 2.00 mmol) in anhydrous DMF (10 mL) were added 4-aminothiophenol (300 μL, 2.40 mmol) and triethylamine (333 μL, 2.40 mmol). The mixture was stirred for 20 h at 0 °C under nitrogen atmosphere in a closed container, and then precipitated from ethyl acetate. The solid was collected, dried at room temperature, re-dissolved in dichloromethane, and washed with brine. The organic extracts were dried over Na_2SO_4, filtered and concentrated. The concentrated solution was purified by precipitation from diethyl ether to afford the pure IR830-B-NH_2 chloride as green powder (1.288 g, yield 91%), 99.1% pure by HPLC, RT 14.72 min. ^{1}H NMR (400 MHz, DMSO-d_6): δ 8.85 (d, 2H, *J* = 14.4 Hz), 8.27 (d, 2H, *J* = 8.4 Hz), 8.06 (t, 4H, *J* = 8.6 Hz), 7.75 (d, 2H, *J* = 8.9 Hz), 7.62 (t, 2H, *J* = 7.2 Hz), 7.49 (t, 2H, *J* = 7.5 Hz), 7.09 (d, 2H, *J* = 8.6 Hz), 6.56 (d, 2H, *J* = 8.5 Hz), 6.31 (d, 2H, *J* = 14.4 Hz), 5.25 (s, 2H), 3.76 (s, 6H), 2.74 (t, 4H, *J* = 4.8 Hz), 1.87 (m, 14H) ppm. ^{13}C NMR (100 MHz, DMSO-d_6): δ 173.36, 151.84, 147.14, 144.21, 140.41, 133.27, 133.00, 131.29, 130.18, 129.83, 128.58, 127.62, 127.39, 124.71, 122.22, 121.40, 115.37, 111.59, 101.39, 50.34, 31.65, 26.79, 25.88, 20.64 ppm. MALDI-TOF-MS (ES$^+$): *m*/*z* calcd for [M-Cl]$^+$, 672.34; found, 672.4.

2.6. Synthesis of IR830-NHS chloride

To a solution of IR830-COOH (1.379 g, 2.00 mmol) in dichloromethane (10 mL) were added N-hydroxysuccinimide (NHS) (460 mg, 4.00 mmol) and N,N′-dicyclohexylcarbodiimide (DCC) (824 mg, 4.00 mmol). The mixture was stirred under nitrogen at room temperature for 20 h in a closed container, then the insoluble particulates were filtered off. The solution was washed with brine and the organic extracts were dried over Na_2SO_4, filtered, and concentrated. The concentrated solution was precipitated from diethyl ether twice to afford IR830-NHS chloride as green powder. The solid material was purified by silica gel column chromatography [The eluent was chloroform:methanol = 10:1 (V/V)] (1.238 g, yield 79%), 90.5% pure by HPLC, RT 9.94 min. ^{1}H NMR (400 MHz, DMSO-d_6): δ 8.79 (d, 3H, *J* = 14.4 Hz), 8.79 (d, 2H, *J* = 14.4 Hz), 8.30 (d, 2H, *J* = 8.5 Hz), 8.08 (t, 4H, *J* = 8.8 Hz), 7.77 (d, 2H, *J* = 8.9 Hz), 7.66 (t, 2H, *J* = 7.3 Hz), 7.51 (t, 2H, *J* = 7.3 Hz), 6.35 (d, 2H, *J* = 14.4 Hz), 3.79 (s, 6H), 3.16 (d, 2H, *J* = 5.7 Hz), 3.11 (d, 2H, *J* = 5.5 Hz), 2.81 (s, 4H), 2.71 (s, 4H), 2.05–1.81 (m, 14H) ppm. ^{13}C NMR (100 MHz, DMSO-d_6): δ 173.63, 170.09, 167.43, 152.74, 143.39, 140.54, 133.18, 132.79, 131.38, 130.25, 129.92, 127.71, 127.46, 124.78, 122.20, 111.65, 101.40, 50.41, 31.81, 31.44, 26.78, 25.80, 25.50, 20.57 ppm. MALDI-TOF-MS (ES$^+$): *m*/*z* calcd. for [M-Cl]$^+$, 750.98; found, 750.7.

2.7. Synthesis of IR830-PEG5K

A mixture of IR830-NHS chloride (188.5 mg, 0.24 mmol) and mPEG5K-NH_2 (1.000 g, 0.20 mmol) was dissolved in DMF (10 mL) and stirred under nitrogen at room temperature for 24 h in a closed container. The mixture was purified through dialysis by transferring the mixture to a dialysis bag (MWCO: 3500) and immersing it in DMF (250 mL). The dialysis fluid was replaced every two hours until it was no longer green in color. The retained fluid was precipitated from diethyl ether. The pure solid was collected, and dried at room temperature to give a green powder (1.02 g, yield 88%). The loading content of the IR830-NHS in the polymer was 7.5 wt.% as determined by UV–vis spectroscopy. HPLC (eluent A/B = 50/50 – 40 min – 0/100; flow rate = 1.0 mL/min), RT 2.24 min.

2.8. Synthesis of PLG-g-mPEG/IR830

To a solution of PLG-g-mPEG (500 mg) in DMF (10 mL) were added 1-ethyl-3-(3-dimethylaminopropyl)carbodiimide (15.3 mg, 0.080 mmol) and 1-hydroxybenzotriazole (10.8 mg, 0.080 mmol). The mixture was stirred at room temperature for 20 min, then IR830-B-NH_2 chloride (28.32 mg, 0.04 mmol) and 4-dimethylaminopyridine (10.0 mg, 0.08 mmol) were added. The mixture was stirred at room temperature for 20 h, and then the whole was transferred to a dialysis bag (MWCO: 7000), immersed in a mixture of DMF and deionized water (V/V = 1:1) until the dialysis fluid was colorless, after which the retained fluid was continue dialyzed in deionized water (2L × 5). The retained fluid was collected and freeze-dried under vacuum (488 mg, yield 92.4%). The loading content was 1.75 wt.%, determined by UV–vis spectroscope. HPLC (eluent A/B = 50/50 – 40 min – 0/100; flow rate = 1.0 mL/min), RT 1.64 min.

2.9. Animal model

Male Balb/C nude mice (6-8 weeks old, 16-18 g) were purchased from Beijing Huafukang Biological Technology Co. Ltd. (HFK Bioscience, Beijing). All animal experiments were performed in compliance with the Guidelines for the Care and Use of Research Animals established by the Jilin University Animal Studies Committee.

2.10. Multispectral Optoacoustic Tomography (MSOT) Imaging

Briefly, either the mouse or phantom is placed in a horizontal position in an animal holder that allows for translation of the mouse/phantom through the imaging plane using a linear stage. This position also enables the imaging of multiple cross-sections for 3-dimensional volume reconstructions. In phantom studies, the phantom was imaged at the respective maximum absorption wavelength of dyes at the cross-section. The mice are kept under isoflurane anesthesia. After subcutaneous injection of ICG and IR830-PEG5K into the mice, they were imaged at 779 and 818 nm in 100 μm step size with 1 frame (4 Avg.) per wavelength. For mice with injection of PLG-g-PEG/IR830 via tail vein, the mice were imaged at 680, 760, 800, 832, 850 and 900 nm using 1 frame (4 Avg.) per wavelength to allow for multispectral unmixing of hemoglobin and injected PLG-g-PEG/IR830. The raw signals were reconstructed using a model-based inversion algorithm and specific signals were spectrally resolved by the pseudo-inverse unmixing method as implemented in the ViewMSOT software (iThera Medical, GmbH, Neuherberg, Germany).

Phantom was prepared according to the Protocol provided by iThera Medical. Agar was used to give phantom rigidity. Intralipid was used to produce tissue-like scattering. After 1.5 g agar and 5 ml 20% intralipid in 98.5 g water was heated to boiling in a beaker, allowing the mixture to cool. When the mixture was approximately 50 °C, pour 10 ml into a 20 cc syringe so that the solution would solidify as a cylinder. Cut a straw to 4 cm in length, and seal one side with glue. Submerge the straw in the center of the phantom. The straw should not be completely submerged. In this way, when the phantom solidified, a probe of interest could be added into the straw for phantom test.

2.11. Lowest Limit of Quantification (LLOQ)

The LLOQ calculations were according to ICHHT Guideline.

The LLOQ is expressed as:

$$\mathrm{LLOQ} = \frac{10\sigma}{S}$$

where, σ = the standard deviation of the background response of blank samples; S = the slope of the calibration curve. The slope S was estimated from the calibration curve of the analyte. The estimation of σ was carried out based on standard deviation of the blank solution. Measurement of the magnitude of analytical background response was performed by analyzing an appropriate number of blank samples and calculating the standard deviation of these responses.

2.12. In vitro cytotoxicity

The *in vitro* cytotoxicity of the samples were tested against the fibroblasts cell line L929 by MTT [3-(4′,5′-dimethylthiazol-2′-yl)-2,5-diphenyltetrazolium bromide] assay. The L929 cells were grown at 37 °C in a humidified atmosphere of 5% CO_2 in Dulbecco modified Eagle medium (DMEM). The culture medium was supplemented with 10% fetal calf serum, 100 μg/mL streptomycin, 100 U/ml penicillin and 4.00 mM L-glutamine. The cells were seeded in 96-well plates at a density of 7000 cells per well. The cells were incubated at 37 °C for 24 h with 100 μL of culture medium containing a series of doses of the samples. After the incubation, the culture medium in each well was removed and the cells were washed three times with PBS. Then, the MTT solution (20 μL, 5 mg/mL) was added to each well and cultured for another 4 h. The supernatant was discarded and then 150 μL of DMSO was added to each well. The absorbance of the solution was measured with a Bio-Rad 680 microplate reader at 492 nm. The results were shown as the viable percentage of cells subjected to various treatments relative to the control cells without any treatment.

2.13. Statistical analysis

Data are expressed as the mean ± STD. Statistical significance was determined using the Student's *t*-test. $P < 0.05$ was considered statistically significant.

3. Results and discussion

3.1. Syntheses of functional IR830 dyes

IR830 chloride was firstly prepared from IR830 *p*-toluenesulfonate by the ion exchange reaction. IR830-COOH and IR830-B-NH_2 chloride were then prepared from IR830 chloride through nucleophilic substitution reactions. IR830-NHS chloride was prepared by the reaction of IR830-COOH chloride with NHS (Scheme 1). The chemical structures and high purities of the obtained functional IR830-based dyes were confirmed by ^1H NMR, ^{13}C NMR, MALDI-TOF-MS and HPLC (Fig. S1–S7).

3.2. UV–vis and fluorescence spectra of functional IR830 dyes

As compared with ICG at the same concentration, the IR830 series dyes display almost the same level of signal intensity in the near-infrared region of UV–vis absorption spectra (Fig. 1a), but negligible signals in the fluorescence spectra (Fig. 1b). This indicates that the IR830 series dyes will have lower fluorescence emission-induced energy loss during the light-heat energy conversion in PAI, compared to the ICG.

3.3. MSOT spectrum of functional IR830 dyes

The *in vitro* photoacoustic signal intensities of the IR830 series dyes and ICG were compared in a phantom. The phantom is a cylindrical model made from agar with a cylindrical hole in the centre which can mimic the *in vivo* tissue environment of animals [35]. Image acquisition, data acquisition and analysis were performed on a multispectral optoacoustic tomography (MSOT) scanner at the maximum absorption wavelengths of the dyes from the cross-section of the phantom. The single wavelength MSOT images at the cross-section of the phantom injected with different concentration of dyes are shown in Fig. S8. A linear relationship was observed between photoacoustic signal intensity and concentration of the IR830 series dyes (Fig. 2), indicating that PAI can be used for quantitative analysis of the dyes. The slopes of linear fit lines of IR830 series dyes are 1.8–2.1 folds greater than that of ICG. The Lowest Limit of Quantification (LLOQ) of the IR830 series dyes is in the range of 0.0125–0.0377 μM, much lower than that of ICG (0.0894 μM) (Table 1). These results demonstrate that the IR830 series dyes are much more efficient than ICG for PAI.

3.4. Photoacoustic profile of IR830-PEG5K

In order to verify whether IR830-COOH and IR830-NHS chloride can be used for labelling polymeric biomaterials in *in vivo* PAI,

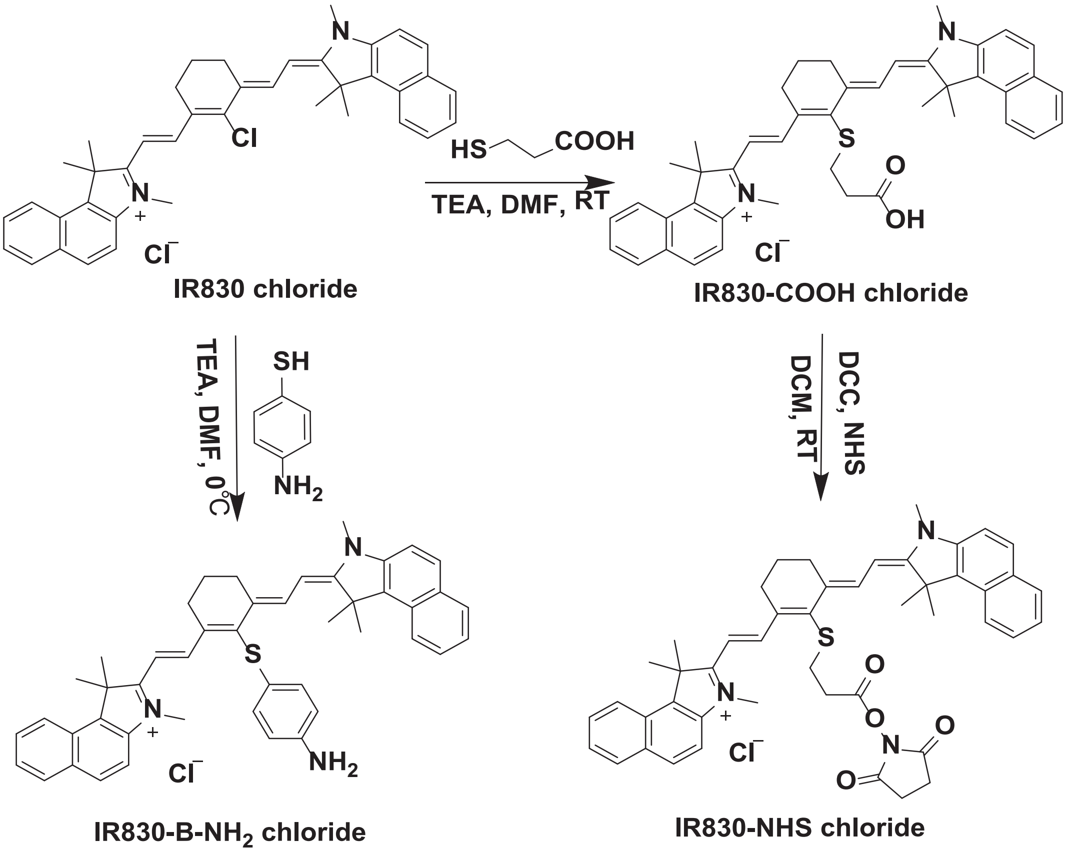

Scheme 1. Syntheses of IR830-COOH, IR830-B-NH_2 and IR830-NHS chloride.

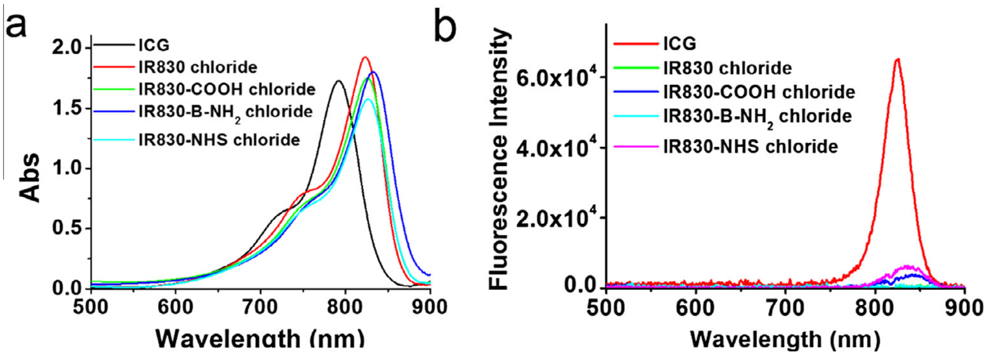

Fig. 1. (a) UV–vis absorption spectroscopy and (b) fluorescence spectroscopy of ICG, IR830 chloride, IR830-COOH chloride, IR830-B-NH$_2$ chloride and IR830-NHS chloride. Each dye was dissolved in DMF at a concentration of 10 μM. Excitation (ICG) = 792 nm, Excitation (IR830 chloride) = 823 nm, Excitation (IR830-COOH chloride) = 826 nm, Excitation (IR830-B-NH$_2$ chloride) = 832 nm, Excitation (IR830-NHS chloride) = 826 nm.

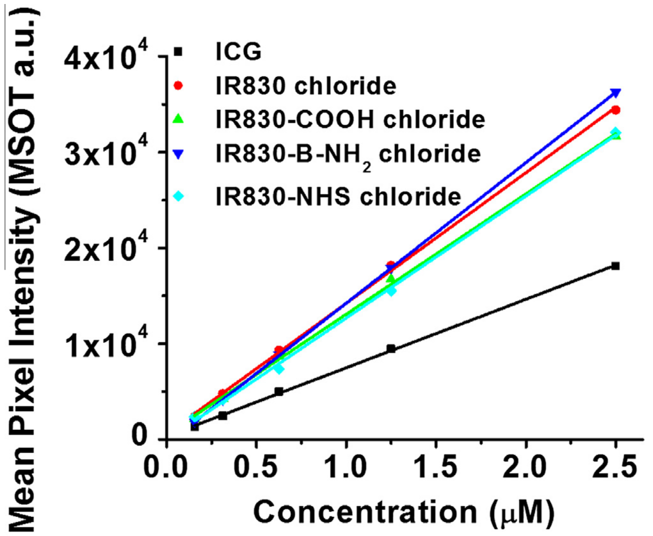

Fig. 2. Signal intensity versus concentration of dyes in MSOT phantom tests. The signal intensity was acquired by the Single wavelength, Single x-section mode. Each dye was dissolved in ethanol. Excitation (ICG) = 792 nm, Excitation (IR830 chloride) = 823 nm, Excitation (IR830-COOH chloride) = 826 nm, Excitation (IR830-B-NH$_2$ chloride) = 832 nm, Excitation (IR830-NHS chloride) = 826 nm.

Table 1
MSOT property of ICG and IR830 series dyes.

Dye	Slope (MSOT a.u./μM)[a]	Slope$_{[Dye]}$/ Slope$_{[ICG]}$	LLOQ (μM)	LLOQ $_{[ICG]}$/ LLOQ$_{[Dye]}$
ICG	7147.4	1.0	0.0894	1.0
IR830 chloride	13631.2	1.9	0.0326	2.7
IR830-COOH chloride	12552.1	1.8	0.0377	2.4
IR830-B-NH$_2$ chloride	14669.3	2.1	0.0125	7.2
IR830-NHS chloride	12726.1	1.8	0.0372	2.4

[a] The slope of the Linear Fit of Mean Pixel Intensity versus concentration of dyes in MSOT phantom tests according to Fig. 2.

IR830-PEG5K was prepared through the reaction of IR830-NHS chloride with mPEG5K-NH$_2$. Signal of IR830 moiety is clearly shown in the ^{1}H NMR of the obtained IR830-PEG5K (Fig. S9). Single peak is displayed in the HPLC spectrum of the IR830-PEG5K (Fig. S7), indicating the high purity of the conjugate. The IR830-PEG5K is water soluble and has weaker near-infrared absorption in water than in DMF (Fig. S10A). The MSOT signal intensity of ICG is much lower in water (slope of linear fit line: 2353.1 MSOT a.u./μM, Fig. S10B) than in ethanol (slope of linear fit line: 7147.4 MSOT a.u./μM, Fig. 2). The slope of linear fit line of the IR830-PEG5K in water is 3236.3 MSOT a.u./μM (Fig. S10B), which is 1.4 folds of ICG in water. Considering that serum proteins could bind cyanine dyes such as ICG and IR830 dyes, the UV–vis absorption and fluorescence spectroscopy of ICG (10 μM) and IR830-PEG5K (10 μM on the IR830 basis) were measured in 20% (v/v) fetal calf serum solution. As shown in Fig. S10C, the IR830-PEG5K displayed much lower fluorescence brightness as compared with the ICG. For *in vivo* evaluation, identical amounts (100 μM, 20 μL) of ICG and IR830-PEG5K were subcutaneously injected into the back of a nude mouse. Image acquisition, data acquisition and analysis were performed by MSOT at the maximum absorption wavelength for the two compounds (779 nm for ICG, 818 nm for IR830-PEG5K) (Fig. 3a). The signal vs. position curves were determined by region of interest (ROI) analysis as implemented in ViewMSOT™. The height (Δ) of peaks represented the MSOT signal intensity of dyes. The height of peaks in the IR830-PEG5K ROI (Δ = 7300) was 1.9-folds of that of the ICG (Δ = 3907) (Fig. 3b), confirming the high efficiency of the IR830-PEG5K. Considering that both the NHS and carboxylic acid derivatives will lead to the formation of similar conjugates depending on the coupling mechanism, these results indicate that IR830-COOH and IR830-NHS chloride can be used as high efficiency photoacoustic dyes for labelling polymeric biomaterials in *in vivo* PAI.

3.5. Photoacoustic profile of PLG-g-mPEG/IR830

To evaluate whether IR830-B-NH$_2$ chloride can be used for *in vivo* PAI, poly(L-glutamic acid)-g-methoxy poly(ethylene glycol) (PLG-g-mPEG) was labelled with IR830-B-NH$_2$ chloride. Signal of IR830 moiety appears in the ^{1}H NMR of the obtained PLG-g-mPEG/IR830 (Fig. S11). Single peak is displayed in the HPLC spectrum of the PLG-g-mPEG/IR830 (Fig. S7), suggesting the high purity of the conjugate. The loading content of the IR830-B-NH$_2$ chloride in the obtained PLG-g-mPEG/IR830 was 1.75 wt.%, as determined by UV–vis spectroscopy (Fig. S12). A plot of MSOT signal intensity of IR830-PEG5K, PLG-g-mPEG/IR830 and ICG in 20% (v/v) fetal calf serum solution in phantom tests is shown in Fig. S13. The slopes of linear fit line of the IR830-PEG5K and PLG-g-mPEG/IR830 are 2.1–2.4 folds of that of ICG, indicating that the IR830 dyes have higher efficiency than ICG in photoacoustic imaging. Before and after 1, 2, 4, 8, 12, 18, 24, 48 h of intravenous administration of PLG-g-mPEG/IR830 via tail vein (200 μL × 25 μM per mouse on the basis of IR830), 3D overview MSOT images were acquired at multiple wavelengths and multiple x-sections in 100 μm steps (Fig. 4). During the first few hours after injection, the MSOT signal intensity in the liver region increased gradually,

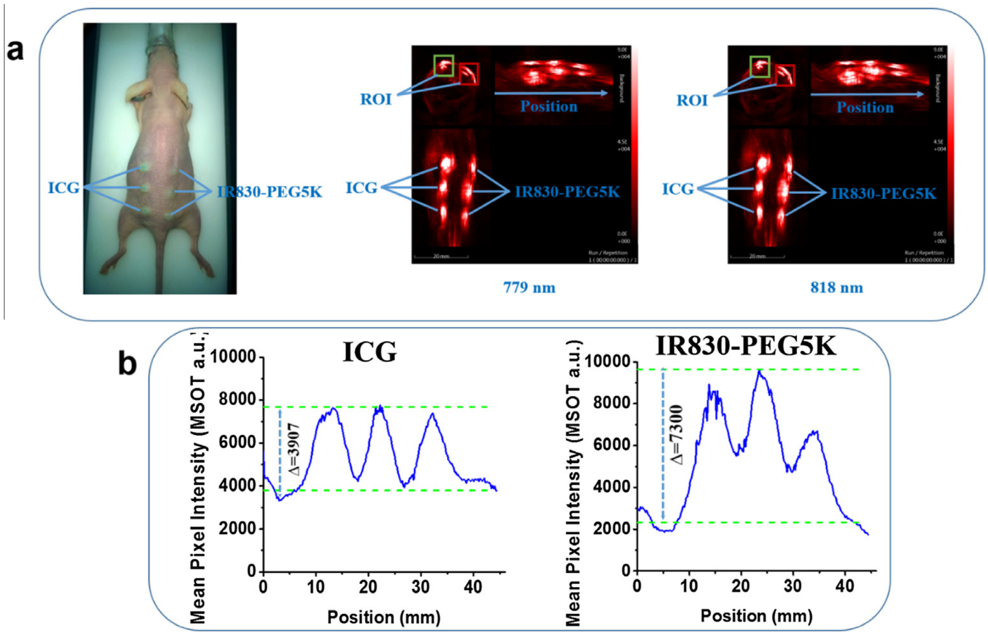

Fig. 3. (a) 3D MSOT overview image of mice model after subcutaneous injection of identical amounts (100 μM, 20 μL) of ICG and IR830-PEG5K into the dorsiventral opposite position of nude mice. Image acquisition and analysis were performed at the respective maximum absorption wavelength of the dyes (779 nm for ICG, 818 nm for IR830-PEG5K). Data were reconstructed using ViewMSOT™ and images at different wavelength were exported as TIFF sequence file. (b) MSOT signal intensity of ICG and IR830-PEG5K in ROI versus positions. ICG data were acquired at the wavelength of 779 nm and IR830-PEG5K data were acquired at 818 nm.

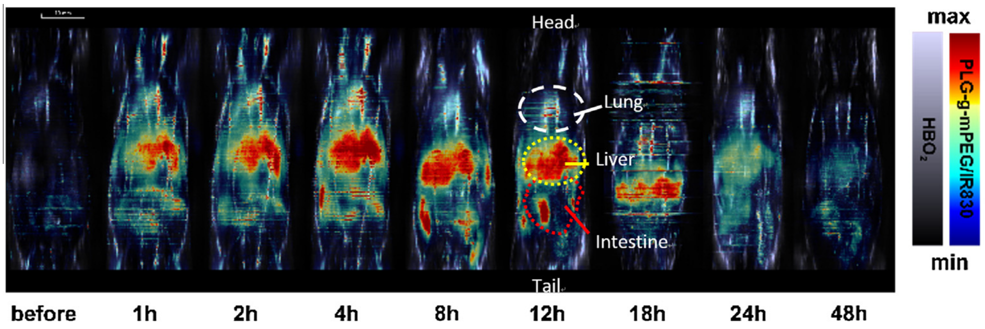

Fig. 4. The x-z overview MSOT image of mice acquired by multispectral data analysis before and after intravenous injection of PLG-g-mPEG/IR830 via tail vein.

until it reached a maximum value at 4 h, which revealed that the IR830-labelled polymers mainly accumulated in the liver post-administration. A clear liver-gastrointestinal metabolic pathway was observed afterwards. The MSOT signal intensity in the intestinal region increased while the liver signal intensity gradually weakened. After 48 h, the whole-body signal intensity reduced to a low level, indicating that most of the PLG-g-mPEG/IR830 had been metabolized. These suggest that the IR830-B-NH_2 chloride can be used for *in vivo* PAI.

3.6. Cytotoxicity of IR830-labelled polymers

The *in vitro* cytotoxicity of the IR830-labelled polymer was evaluated with MTT assays. As shown in Fig. 5, the L929 cells treated with the IR830-PEG5K or PLG-g-mPEG/IR830 showed more than 90% viability at all tested concentrations in 24 h, even at 5.0 μM (133–400 fold greater than LLOQ of IR830 series dyes). In particular, the L929 cells treated with the IR830-PEG5K showed 87% viability at 160 μM (1.6-fold of concentration administered *in vivo*) in 24 h (Fig. S14). Thus, the IR830 labelled polymers exhibit very low cytotoxicity.

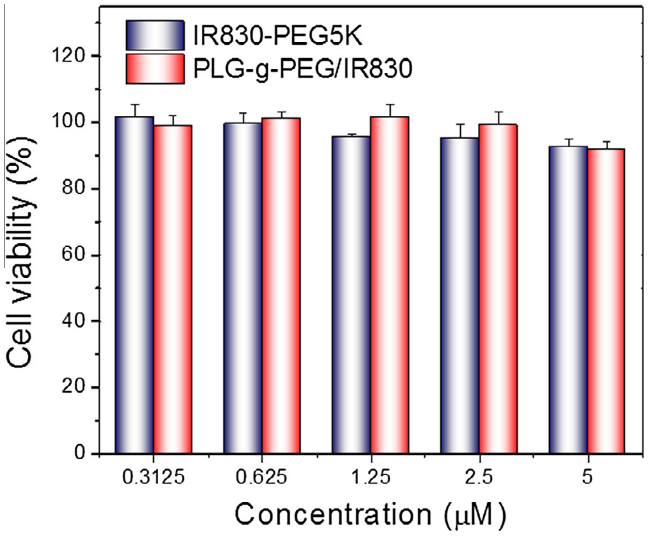

Fig. 5. *In vitro* cytotoxicity of IR830-PEG5k and PLG-g-PEG/IR830 to L929 cells. The concentration is on the IR830 basis. $n = 3$.

4. Conclusion

In summary, we have prepared a series of highly efficient photoacoustic dyes with —COOH, —NH_2 and NHS ester functionalities, from an inexpensive industrial computer-to-plate NIR absorber, IR830 *p*-toluenesulfonate. These functional IR830 dyes have strong near-infrared absorption while displaying low fluorescence, which makes them much more efficient in PAI than ICG. In addition, these functional IR830 dyes can be conveniently used to label polymeric biomaterials with low cytotoxicity. The IR830-COOH chloride, IR830-B-NH_2 chloride and IR830-NHS chloride can be used to conjugate —OH, —COOH and —NH_2 groups, respectively. There is a linear relationship between photoacoustic signal intensity and dye concentration, suggesting that the functional IR830 dyes can be used for quantitative analysis for *in vitro* and *in vivo* PAI. The metabolic process of the polymeric material in mice could be successfully traced by using the functional IR830 dyes. Based on these studies, we believe that the functional IR830 dyes have excellent potential as highly efficient photoacoustic dyes for *in vitro* and *in vivo* applications.

Acknowledgments

This research was financially supported by National Natural Science Foundation of China (Projects 51473029, 51233004, 51373168, 51528303 and 51403204) and the Chinese Academy of Sciences Youth Innovation Promotion Association.

Appendix A. Supplementary data

Supplementary data (^1H and ^{13}C NMR spectra of IR830 chloride, IR830-COOH chloride, IR830-B-NH_2 chloride, and IR830-NHS chloride, MALDI-TOF-MS of IR830-COOH chloride, IR830-B-NH_2 chloride, and IR830-NHS chloride, HPLC of IR830-COOH chloride, IR830-B-NH_2 chloride, IR830-NHS chloride, IR830-PEG5K and PLG-g-mPEG/IR830, MSOT images in phantom tests, ^1H NMR spectra of IR830-PEG5K and PLG-g-mPEG/IR830, plot of MSOT signal intensity versus concentration of dyes, and UV–VIS spectrum of PLG-g-mPEG/IR830, in vitro cytotoxicity of IR830-PEG5k to L929 cells.) associated with this article can be found, in the online version, at http://dx.doi.org/10.1016/j.actbio.2016.07.026.

References

[1] E.I. Galanzha, E.V. Shashkov, T. Kelly, J.W. Kim, L. Yang, V.P. Zharov, In vivo magnetic enrichment and multiplex photoacoustic detection of circulating tumour cells, Nat. Nanotechnol. 4 (2009) 855–860.

[2] L.V. Wang, Multiscale photoacoustic microscopy and computed tomography, Nat. Photonics 3 (2009) 503–509.

[3] X. Wang, Y. Pang, G. Ku, X. Xie, G. Stoica, L.V. Wang, Noninvasive laser-induced photoacoustic tomography for structural and functional in vivo imaging of the brain, Nat. Biotechnol. 21 (2003) 803–806.

[4] E.Z. Zhang, J.G. Laufer, R.B. Pedley, P.C. Beard, In vivo high-resolution 3D photoacoustic imaging of superficial vascular anatomy, Phys. Med. Biol. 54 (2009) 1035–1046.

[5] L.V. Wang, S. Hu, Photoacoustic tomography: in vivo imaging from organelles to organs, Science 335 (2012) 1458–1462.

[6] W. Wu, W. Driessen, X. Jiang, Oligo(ethylene glycol)-based thermosensitive dendrimers and their tumor accumulation and penetration, J. Am. Chem. Soc. 136 (2014) 3145–3155.

[7] A.J. Dixon, S. Hu, A.L. Klibanov, J.A. Hossack, Oscillatory dynamics and in vivo photoacoustic imaging performance of plasmonic nanoparticle-coated microbubbles, Small 11 (2015) 3066–3077.

[8] X. Wu, B. Lin, M. Yu, L. Yang, J. Han, S. Han, A carbohydrate-grafted nanovesicle with activatable optical and acoustic contrasts for dual modality high performance tumor imaging, Chem. Sci. 6 (2015) 2002–2009.

[9] F.-F. An, Z.-J. Deng, J. Ye, J.-F. Zhang, Y.-L. Yang, C.-H. Li, C.-J. Zheng, X.-H. Zhang, Aggregation-induced near-infrared absorption of squaraine dye in an albumin nanocomplex for photoacoustic tomography in vivo, ACS Appl. Mater. Interfaces 6 (2014) 17985–17992.

[10] R.J. Nagao, Y. Ouyang, R. Keller, S.Y. Nam, G.R. Malik, S.Y. Emelianov, L.J. Suggs, C.E. Schmidt, Ultrasound-guided photoacoustic imaging-directed re-endothelialization of acellular vasculature leads to improved vascular performance, Acta Biomater. 32 (2016) 35–45.

[11] T. Bao, W. Yin, X. Zheng, X. Zhang, J. Yu, X. Dong, Y. Yong, F. Gao, L. Yan, Z. Gu, Y. Zhao, One-pot synthesis of PEGylated plasmonic MoO3–x hollow nanospheres for photoacoustic imaging guided chemo-photothermal combinational therapy of cancer, Biomaterials 76 (2016) 11–24.

[12] Y. Jin, Y. Li, X. Ma, Z. Zha, L. Shi, J. Tian, Z. Dai, Encapsulating tantalum oxide into polypyrrole nanoparticles for X-ray CT/photoacoustic bimodal imaging-guided photothermal ablation of cancer, Biomaterials 35 (2014) 5795–5804.

[13] L. Jing, X. Liang, Z. Deng, S. Feng, X. Li, M. Huang, C. Li, Z. Dai, Prussian blue coated gold nanoparticles for simultaneous photoacoustic/CT bimodal imaging and photothermal ablation of cancer, Biomaterials 35 (2014) 5814–5821.

[14] C. Lee, J. Kim, Y. Zhang, M. Jeon, C. Liu, L. Song, J.F. Lovell, C. Kim, Dual-color photoacoustic lymph node imaging using nanoformulated naphthalocyanines, Biomaterials 73 (2015) 142–148.

[15] W. Li, P. Rong, K. Yang, P. Huang, K. Sun, X. Chen, Semimetal nanomaterials of antimony as highly efficient agent for photoacoustic imaging and photothermal therapy, Biomaterials 45 (2015) 18–26.

[16] J. Mou, C. Liu, P. Li, Y. Chen, H. Xu, C. Wei, L. Song, J. Shi, H. Chen, A facile synthesis of versatile Cu2-xS nanoprobe for enhanced MRI and infrared thermal/photoacoustic multimodal imaging, Biomaterials 57 (2015) 12–21.

[17] K. Pu, A.J. Shuhendler, J.V. Jokerst, J. Mei, S.S. Gambhir, Z. Bao, J. Rao, Semiconducting polymer nanoparticles as photoacoustic molecular imaging probes in living mice, Nat Nano 9 (2014) 233–239.

[18] X. Gao, C. Li, Nanoprobes visualizing gliomas by crossing the blood brain tumor barrier, Small 10 (2014) 426–440.

[19] A. De la Zerda, C. Zavaleta, S. Keren, S. Vaithilingam, S. Bodapati, Z. Liu, J. Levi, B.R. Smith, T.J. Ma, O. Oralkan, Z. Cheng, X. Chen, H. Dai, B.T. Khuri-Yakub, S.S. Gambhir, Carbon nanotubes as photoacoustic molecular imaging agents in living mice, Nat. Nanotechnol. 3 (2008) 557–562.

[20] J.W. Kim, E.I. Galanzha, E.V. Shashkov, H.M. Moon, V.P. Zharov, Golden carbon nanotubes as multimodal photoacoustic and photothermal high-contrast molecular agents, Nat. Nanotechnol. 4 (2009) 688–694.

[21] C. Bao, N. Beziere, P. del Pino, B. Pelaz, G. Estrada, F. Tian, V. Ntziachristos, J.M. de la Fuente, D. Cui, Gold nanoprisms as optoacoustic signal nanoamplifiers for in vivo bioimaging of gastrointestinal cancers, Small 9 (2013) 68–74.

[22] P. Huang, J. Lin, W. Li, P. Rong, Z. Wang, S. Wang, X. Wang, X. Sun, M. Aronova, G. Niu, Biodegradable gold nanovesicles with an ultrastrong plasmonic coupling effect for photoacoustic imaging and photothermal therapy, Angew. Chem. 125 (2013) 14208–14214.

[23] K.A. Homan, M. Souza, R. Truby, G.P. Luke, C. Green, E. Vreeland, S. Emelianov, Silver nanoplate contrast agents for in vivo molecular photoacoustic imaging, ACS Nano 6 (2012) 641–650.

[24] D. Pan, X. Cai, C. Yalaz, A. Senpan, K. Omanakuttan, S.A. Wickline, L.V. Wang, G. M. Lanza, Photoacoustic sentinel lymph node imaging with self-assembled copper neodecanoate nanoparticles, ACS Nano 6 (2012) 1260–1267.

[25] G. Ku, M. Zhou, S. Song, Q. Huang, J. Hazle, C. Li, Copper sulfide nanoparticles as a new class of photoacoustic contrast agent for deep tissue imaging at 1064 nm, ACS Nano 6 (2012) 7489–7496.

[26] J. Yu, C. Yang, J. Li, Y. Ding, L. Zhang, M.Z. Yousaf, J. Lin, R. Pang, L. Wei, L. Xu, Multifunctional Fe_5C_2 nanoparticles: a targeted theranostic platform for magnetic resonance imaging and photoacoustic tomography-guided photothermal therapy, Adv. Mater. 26 (2014) 4114–4120.

[27] Q. Fan, K. Cheng, Z. Yang, R. Zhang, M. Yang, X. Hu, X. Ma, L. Bu, X. Lu, X. Xiong, W. Huang, H. Zhao, Z. Cheng, Photoacoustic imaging: perylene-diimide-based nanoparticles as highly efficient photoacoustic agents for deep brain tumor imaging in living mice (Adv. Mater. 5/2015), Adv. Mater. 27 (2015). 774-774.

[28] N. Beziere, N. Lozano, A. Nunes, J. Salichs, D. Queiros, K. Kostarelos, V. Ntziachristos, Dynamic imaging of PEGylated indocyanine green (ICG) liposomes within the tumor microenvironment using multi-spectral optoacoustic tomography (MSOT), Biomaterials 37 (2015) 415–424.

[29] A. Hannah, G. Luke, K. Wilson, K. Homan, S. Emelianov, Indocyanine green-loaded photoacoustic nanodroplets: dual contrast nanoconstructs for enhanced photoacoustic and ultrasound imaging, ACS Nano 8 (2013) 250–259.

[30] W. Song, Z. Tang, D. Zhang, N. Burton, W. Driessen, X. Chen, Comprehensive studies of pharmacokinetics and biodistribution of indocyanine green and liposomal indocyanine green by multispectral optoacoustic tomography, RSC Adv. 5 (2015) 3807–3813.

[31] A. de la Zerda, S. Bodapati, R. Teed, S.Y. May, S.M. Tabakman, Z. Liu, B.T. Khuri-Yakub, X. Chen, H. Dai, S.S. Gambhir, Family of enhanced photoacoustic imaging agents for high-sensitivity and multiplexing studies in living mice, ACS Nano 6 (2012) 4694–4701.

[32] A. Rosencwaig, A. Gersho, Theory of the photoacoustic effect with solids, J. Appl. Phys. 47 (1976) 64–69.

[33] C. Kim, C. Favazza, L.V. Wang, In vivo photoacoustic tomography of chemicals: high-resolution functional and molecular optical imaging at new depths, Chem. Rev. 110 (2010) 2756–2782.

[34] H.Y. Yu, Z.H. Tang, D.W. Zhang, W.T. Song, Y. Zhanga, Y. Yang, Z. Ahmad, X.S. Chen, Pharmacokinetics, biodistribution and in vivo efficacy of cisplatin loaded poly(L-glutamic acid)-g-methoxy poly(ethylene glycol) complex nanoparticles for tumor therapy, J. Control. Release 205 (2015) 89–97.

[35] D. Razansky, A. Buehler, V. Ntziachristos, Volumetric real-time multispectral optoacoustic tomography of biomarkers, Nat. Protoc. 6 (2011) 1121–1129.